Solvent-Tuned Plasticity for Various Binder-Free Applications of a New Lead-Free Manganese Halide

Joo Hyeong Han, Jeong Min Seo, San Ha Choi, Jae Geon Noh, Jeong Wan Min, Yu Ri Kim, Hyeon Woo Kim, Sung Beom Cho, Bo Kyung Cha, and Won Bin Im*

The development of efficient color conversion layers for μ-LED technology faces significant challenges owing to the limitations of materials that require binders. Binders are typically used to ensure uniform film formation in color-conversion layers, but they often cause optical losses, increase layer thickness, and introduce long-term stability issues. To address the limitations of materials requiring binders, cyclopropyltriphenylphosphonium manganese tetrabromide ($CPTP_2MnBr_4$) is synthesized, a novel lead-free metal halide. $CPTP_2MnBr_4$ exhibits unique solvent-based plasticity, which enables the formation of uniform films thinner than those formed with binders without the need for either heat treatment or binders. This approach eliminates the performance degradation typically associated with conventional binder systems such as optical losses and stability issues. Structural and optical analyses confirm its high luminescence efficiency and stability, supporting its potential applications in luminescent clays, direct ink writing, pattern printing, and ink drawing. Moreover, its successful application in white light-emitting diodes (WLEDs) and scintillators demonstrates that $CPTP_2MnBr_4$ can replace traditional binder systems, offering a solution to overcome the technical challenges in next-generation displays, lighting, and scintillator technologies.

1. Introduction

The development of new materials that combine high efficiency and stability has emerged as a critical challenge for luminescent materials. In particular, micro light-emitting diode (μ-LED) technology has gained attention as a next-generation display technology owing to its advantages such as high efficiency, long lifespan, and low power consumption. However, the commercialization and large-scale application of μ-LEDs still face several challenges. Among these, the implementation of high-quality color-conversion layers is a key technical issue because efficient and uniform production of color-conversion materials is crucial.[1]

In this context, perovskite materials have attracted significant interest because of their excellent light-emitting properties and tunable bandgap.[2] However, despite the outstanding optical performance of the widely used lead-based perovskite materials, the toxicity of lead has raised serious environmental and health concerns. Pb is a toxic substance that can harm ecosystems and humans, particularly during the mass production and disposal of electronic products, leading to severe environmental pollution.[3] To address these issues, lead-free metal-halide materials have recently gained attention. These materials, which include metals such as copper, silver, and bismuth, are not only environmentally friendly but also maintain high light-emitting efficiency, making them promising for various applications, including color-conversion layers.[4]

However, the application of these materials typically requires binders (e.g., such as resins and polydimethylsiloxane [PDMS]). Binders are essential for ensuring uniform distribution and film formation, particularly when applying new materials, such as lead-free metal halides. For instance, in color-conversion layers, binders help maintain consistent optical properties and ensure the homogeneity of the material, thereby enhancing the light-emitting efficiency.[5] Despite these benefits, binders have several limitations. The difference in refractive index between the binder and active material can lead to optical losses, and as the amount of binder increases, the color conversion layers and scintillator films may become unnecessarily thick, which can slow down the response time of the device and reduce the energy efficiency.[6] Additionally, chemical interactions between the binder and active material can lead to long-term stability issues, posing significant obstacles to the development of high-performance light-emitting materials.[7] New approaches are required to overcome these challenges.

This study proposes a novel approach to address these limitations by utilizing the solvent-based plasticity of $CPTP_2MnBr_4$
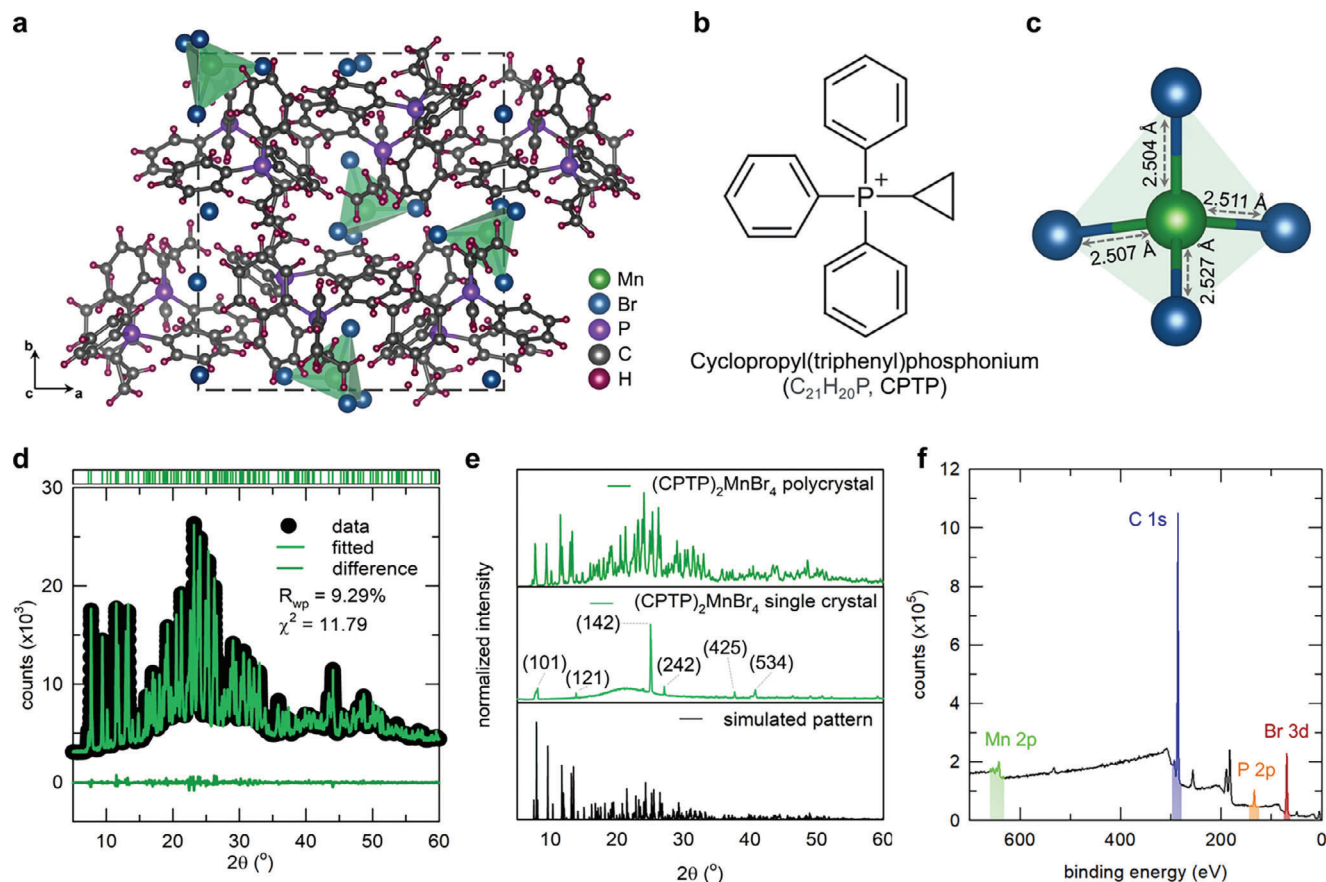
J. H. Han, J. M. Seo, S. H. Choi, J. G. Noh, J. W. Min, Y. R. Kim, W. B. Im
Division of Materials Science and Engineering
Hanyang University
222 Wangsimni-ro, Seongdong-gu, Seoul 04763, Republic of Korea
E-mail: imwonbin@hanyang.ac.kr
H. W. Kim, S. B. Cho
Department of Materials Science and Engineering
Ajou University
Suwon-si, Gyeonggi-do 16499, Republic of Korea
B. K. Cha
Precision Medical Device Research Center Korea Electrotechnology
Research Institute (KERI) Ansan
Asan 15588, Republic of Korea

**ADVANCED
SCIENCE NEWS**

www.advancedsciencenews.com

**ADVANCED
MATERIALS**

www.advmat.de

Figure 1. a) Crystal structure of CPTP$_2$MnBr$_4$. b) Molecular structure of CPTP$^+$ cation. c) Tetrahedra of [MnBr$_4$]$^{2-}$. d) Observed (dots), calculated (red), and difference (deep red) profiles obtained after full-pattern Rietveld refinement of CPTP$_2$MnBr$_4$ polycrystalline phase. e) Comparison of PXRD patterns of single crystal and polycrystalline phase. f) Full-range XPS spectra of the different elements of CPTP$_2$MnBr$_4$.

(CPTP$^+$ = cyclopropyltriphenylphosphonium), a new lead-free metal halide material, to form uniform films without the need for binders or additional heat treatment. This study successfully demonstrates the application of CPTP$_2$MnBr$_4$ as a color-conversion layer in blue LED-based WLEDs, providing a foundation for its potential use in µ-LEDs and other display technologies. This method optimizes the material thickness and maximizes the light-emitting efficiency while preventing performance degradation caused by binder use in color-conversion layers and scintillators. The proposed approach has the potential to address the technical limitations of binders across various industries, including displays, lighting, and scintillators. By eliminating the need for binders, this method simplifies the production process while enabling the fabrication of thinner, more efficient, and stable films. These advantages make this material a promising candidate for next-generation technologies, including advanced displays and lighting systems.
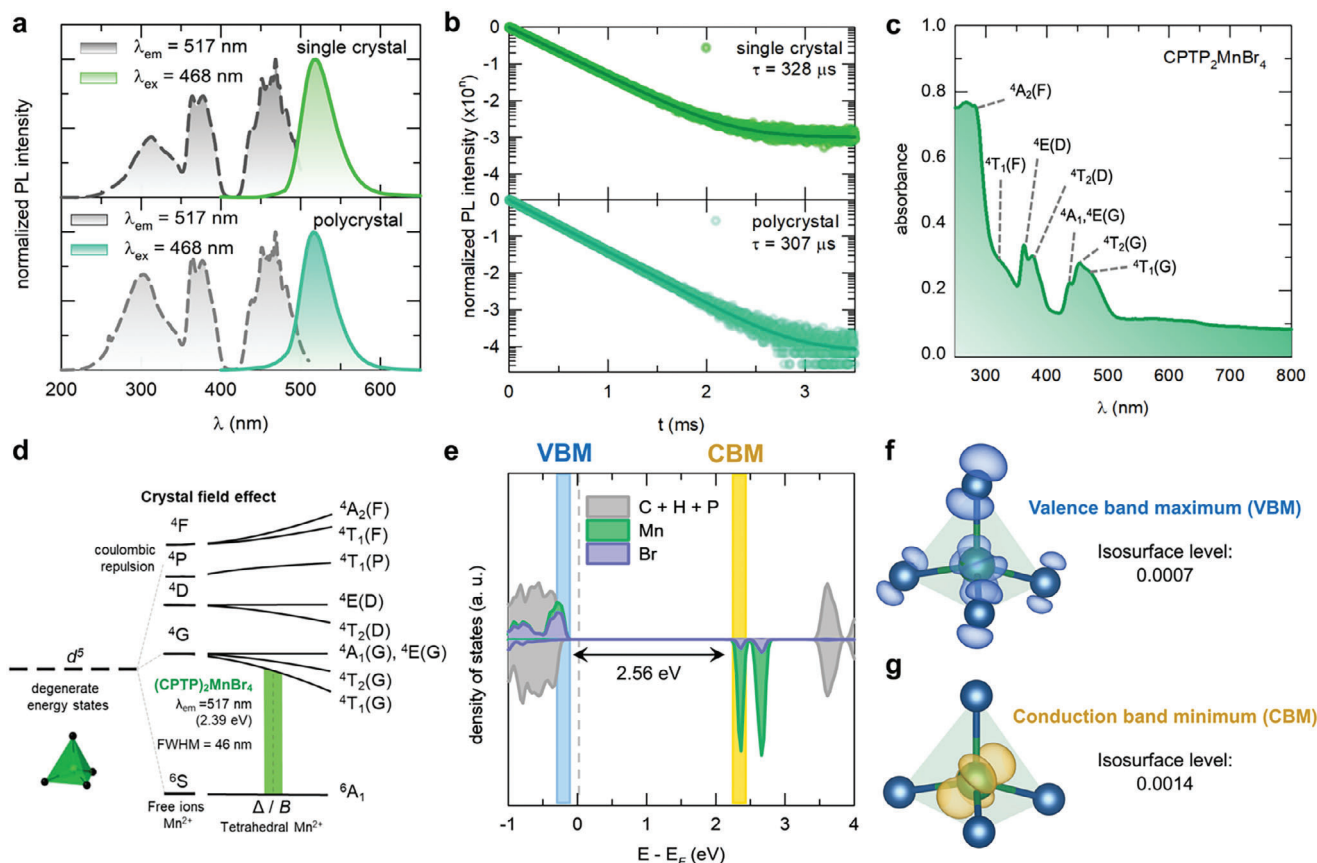
2. Results and Discussion

Single crystals of CPTP$_2$MnBr$_4$ (CPTP$^+$ = cyclopropyltriphenylphosphonium, C$_{21}$H$_{20}$P) were synthesized using an antisolvent vapor-assisted crystallization method. The detailed synthesis steps are shown in Figure S1 (Supporting Information). For fur-

ther structural analysis, single-crystal X-ray diffraction (SC-XRD) was performed, and the resulting crystal structure is shown in **Figure 1a** and Figure S2 (Supporting Information). SC-XRD is essential for determining the atomic arrangement within a crystal and providing precise data on the lattice parameters and symmetry.

The crystal belongs to the $P2_12_12_1$ space group, indicating an orthorhombic structure, with lattice parameters $a = 14.82$ Å, $b = 16.26$ Å, $c = 17.08$ Å, and $\alpha = \beta = \gamma = 90°$. The Mn^{2+} ion is coordinated with four Br$^-$ ions to form a tetrahedral [MnBr$_4$]$^{2-}$ complex, isolated in a 0D structure by the large CPTP$^+$ monovalent cation, as shown in Figure 1b,c. Van der Waals interactions between the CPTP$^+$ cations and [MnBr$_4$]$^{2-}$ tetrahedra help maintain the spatial separation between the tetrahedra.

The polycrystalline phase of CPTP$_2$MnBr$_4$ was synthesized using the mechanochemical method shown in Figure S3 (Supporting Information). The precursors, CPTPBr and MnBr$_2$, were mixed in a 2:1 molar ratio in an agate mortar, followed by the addition of anhydrous ethanol. The mixture was ground for ≈5 min to yield a polycrystalline phase. Powder X-ray diffraction (PXRD) and Rietveld refinement were used to verify the identity of the material using the crystal structure as a reference. The refinement results confirmed that the PXRD patterns fully converged with the expected structural model, demonstrating the successful

Figure 2. a) PL and PLE spectra of single crystal and polycrystalline CPTP$_2$MnBr$_4$ b) Luminescence decay curves of single crystal and polycrystalline CPTP$_2$MnBr$_4$. c) UV–Vis absorption spectrum showing multiple electronic transitions. d) Luminescence mechanism of CPTP$_2$MnBr$_4$. e) Band structure of CPTP$_2$MnBr$_4$. f) VBM, g) CBM in density of states analysis.

synthesis, as shown in Figure 1d. A comparison of the powder XRD patterns of the polycrystalline and single-crystal forms revealed differences in the peak intensities but consistent peak positions, indicating that both phases shared the same crystal structure. The powder XRD pattern of the single crystal demonstrates preferential growth along the (142) plane, as shown in Figure 1e. X-ray photoelectron spectroscopy (XPS) was employed to investigate the elemental composition of CPTP$_2$MnBr$_4$. As shown in Figure 1f, XPS reveals peaks corresponding to C, P, Mn, and Br. Peaks for C 1s (281–295 eV), Mn 2p (634–647 eV), P 2p (128–137 eV), and Br 3d (64–72 eV) are observed. The C 1s peak exhibits the highest intensity, which is attributed to the three benzene rings of the CPTP$^+$ cation. Scanning electron microscopy–energy dispersive spectrometry (SEM–EDS) measurements are performed to confirm the morphology and elemental composition of the synthesized material, as shown in Figure S4 (Supporting Information). EDS analysis identified all the constituent elements, verifying the proper synthesis of the composition.

The photoluminescence (PL) and photoluminescence excitation (PLE) spectra of the polycrystalline and single-crystal phases of CPTP$_2$MnBr$_4$ are compared in **Figure 2a**. Both forms showed PL emission at λ_{em} = 517 nm, with λ_{ex} = 468 nm, and a full-width at half maximum (FWHM) of 46 nm. Three bands are observed in the PLE spectra, corresponding to the transitions from Mn^{2+}'s

4F, 4P, and 4D energy states. Notably, the similarities between the PL and PLE spectra of both forms indicate that they share the same crystal phase.

To investigate the emission mechanism further, time-correlated single-photon counting (TCSPC) measurements were conducted, and the results are shown in Figure 2b. The luminescence decay was well-fitted by a single exponential for both forms, indicating that the emission arises solely from the Mn^{2+} $^4T_1 \rightarrow {}^6A_1$ transition. The single crystal exhibited a longer lifetime (328 µs) compared to the polycrystalline form (307 µs), which suggests fewer structural defects and, consequently, fewer nonradiative recombination pathways. This is consistent with photoluminescence quantum yield (PLQY) values of 83.42% for the single crystal and 62.80% for the polycrystalline phase, as illustrated in Figure S5 (Supporting Information).

In comparison with lead-free double perovskites, such as Cs$_2$Ag$_{1-x}$K$_x$In$_{0.875}$Bi$_{0.125}$Cl$_6$,[8] which are materials frequently studied for WLED and scintillator applications, CPTP$_2$MnBr$_4$ exhibits promising optical properties. Double perovskites typically achieve a maximum PLQY of ≈15.96% under optimized conditions, but they often face challenges related to phase stability and relatively broad emission spectra. In contrast, CPTP$_2$MnBr$_4$ demonstrates a notably higher PLQY of 83.42% in the single-crystal phase, coupled with a sharp emission peak at 517 nm

(FWHM: 46 nm), which may provide an advantage in applications requiring color purity.

In 0D hybrid organic–inorganic manganese bromides, the distance between Mn^{2+} ions plays a crucial role in determining the PLQY.[9] The proximity of Mn^{2+} ions can result in concentration quenching, which lowers the luminescence efficiency through energy transfer. A high PLQY was achieved by maintaining an optimal distance between the Mn^{2+} ions, and in $CPTP_2MnBr_4$, the large $CPTP^+$ cations ensured adequate spacing between the $[MnBr_4]^{2-}$ tetrahedra. The closest Mn–Mn distance in $CPTP_2MnBr_4$ was measured at 9.21 Å, correlating with previous findings on Mn–Mn distance and PLQY, as demonstrated in Figures S6 and S7 (Supporting Information).

Mn^{2+} ions have five unpaired $3d$ electrons, which results in 16 possible L-S term symbols owing to electron–electron repulsion. These include spin sextet ^6S, spin quartets ^4P, ^4D, ^4F, and multiple spin doublets. The different energy states are influenced by the Coulomb interactions and can be described using the Racah parameters B and C. These parameters are calculated as follows:

$$B = \frac{1}{49}\left(F^2 - \frac{5}{4}F^4\right) \tag{1}$$

$$C = \frac{35}{108}F^4 \tag{2}$$

In this equation, F^k ($k = 0, 2, 4$) is used to quantify the electron–electron repulsion within an atom. These values were obtained through quantum mechanical calculations that accounted for the spatial distribution and interactions of electrons. In the case of Mn^{2+} with a d^5 electron configuration, F^2 was ≈ 12000 cm^{-1} and F^4 was ≈ 7500 cm^{-1}. Using these values, the Racah parameters are calculated as follows:

$$B \approx \frac{1}{49}\left(12000 - \frac{5}{4} \times 7500\right) \approx 960\ cm^{-1} \tag{3}$$

$$C \approx \frac{35}{108} \times 7500 \approx 3260\ cm^{-1} \tag{4}$$

For tetrahedrally coordinated Mn^{2+} ions, Coulomb repulsion causes a split into $^6A_1 \rightarrow {^4G}$ and $^6A_1 \rightarrow {^4D}$ transitions5. The energy differences between $^6A_1$ and ^4G and $^6A_1$ and ^4D can be expressed in terms of the Racah parameters 10 B + 5C and 7 B, respectively. Additionally, the d orbitals of Mn at the center experience repulsion owing to the overlap with the four ligands, splitting them into three t_{2g} orbitals and two e_g orbitals. Thus, the originally degenerate d orbitals of Mn, forming a tetrahedron with Br, split into higher-energy t_{2g} and lower-energy e_g orbitals. This phenomenon is known as crystal field splitting, and the extent of splitting is determined by the crystal field strength (Δ).[10]

The positions of the free ion energy levels, considering these three independent variables (B, C, Δ), are determined using the Tanabe–Sugano diagram. This diagram is based on the energy levels of metal ions (E/B) and the crystal field strength (Δ/B). The d^5 Tanabe–Sugano diagram, shown in Figure S8 (Supporting Information), indicates that for Mn^{2+} ions with a weak crystal field strength, the electron transition occurs from $^4T_1$ to $^6A_1$, resulting in green emission in tetrahedral coordination. UV–vis absorption spectroscopy was used to investigate the energy states of $CPTP_2MnBr_4$. The absorption spectrum in Figure 2c reveals multiple distinct peaks corresponding to various electronic transitions. These peaks were located at 284, 326, 363, 379, 456, 471, and 487 nm. The corresponding electronic transitions are $^6A_1 \rightarrow {^4T_1(F)}$, $^6A_1 \rightarrow {^4T_1(P)}$, $^6A_1 \rightarrow {^4E(D)}$, $^6A_1 \rightarrow {^4T_2(D)}$, $^6A_1 \rightarrow {^4A_1(G)}$ and $^4E(G)$, $^6A_1 \rightarrow {^4T_2(G)}$, $^6A_1 \rightarrow {^4T_1(G)}$, respectively. A comprehensive luminescence mechanism is depicted in Figure 2d.

To investigate the photophysical properties of $CPTP_2MnBr_4$, its band structure and density of states (DOS) were theoretically calculated, as shown in Figure 2e. The calculated bandgap was 2.56 eV, which corresponds well with the emission wavelength. As shown in Figure 2f,g, the DOS analysis reveals that the valence band maximum (VBM) and conduction band minimum (CBM) states are formed by the Mn $3d$ and Br $3p$ orbitals. The charge densities, which are equally distributed among Mn^{2+} and Br^- ions, confirm that the electron transitions contributing to the luminescence occur within the $[MnBr_4]^{2-}$ complex.[11]
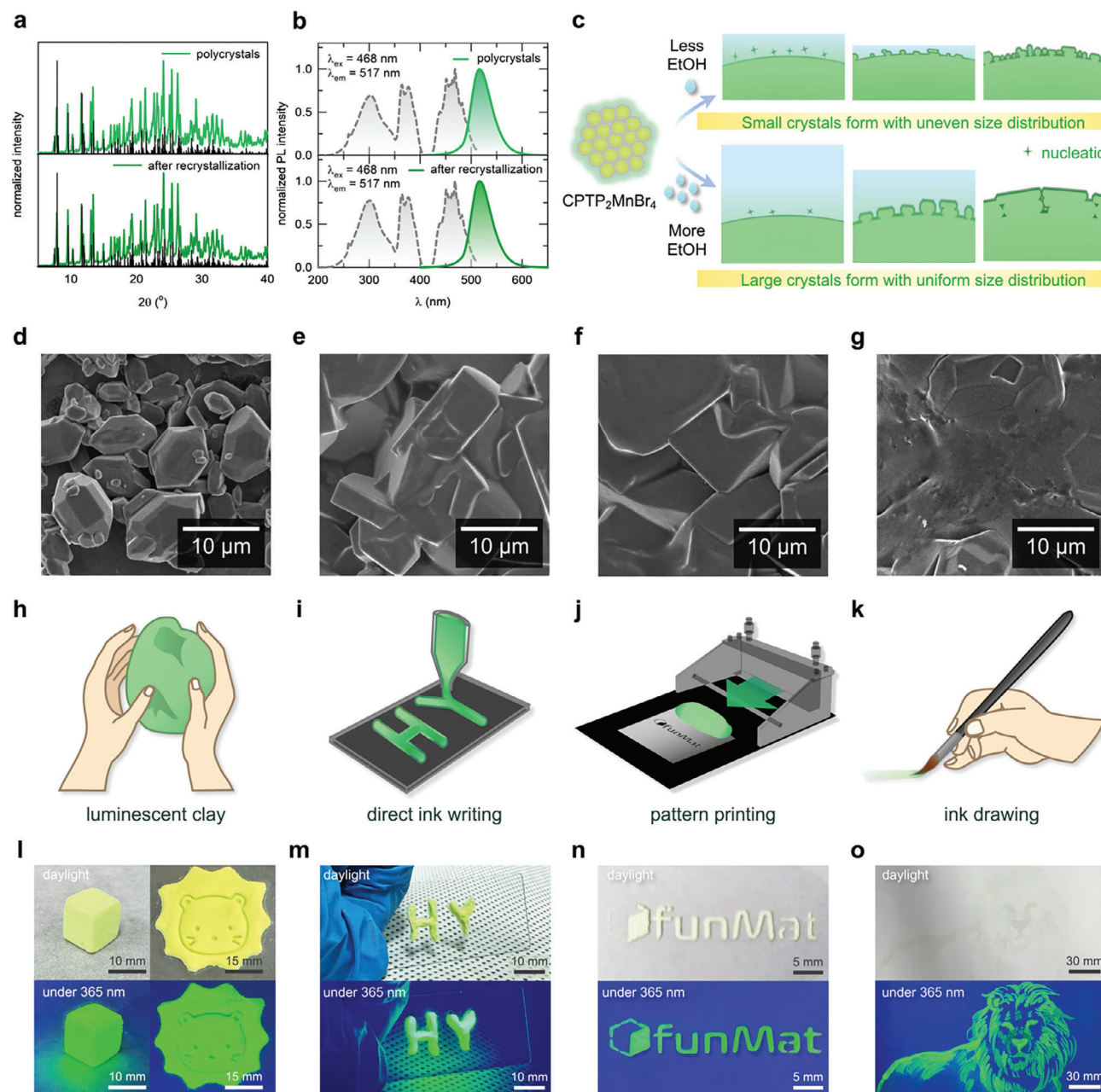
Thermal and chemical stability are crucial properties of luminescent materials. In luminescent materials, an increased temperature leads to reduced luminescence efficiency owing to electron–phonon coupling. To assess the thermal stability of $CPTP_2MnBr_4$, thermal quenching (TQ) was measured up to 150 °C. As shown in Figure S9 (Supporting Information), the material demonstrated excellent thermal stability and maintained more than 90% of its PL intensity at room temperature. In addition, halide-based compositions can decompose in the presence of moisture when exposed to environmental conditions, resulting in the deterioration of their optical properties. Therefore, air stability is a significant indicator for halide-based luminescent materials. The stability of $CPTP_2MnBr_4$ under ambient conditions was evaluated by exposing it to air for 2500 h. As shown in Figure S10 (Supporting Information), the comparison of PL and XRD before and after exposure revealed that $CPTP_2MnBr_4$ maintained its emission wavelength (λ_{em} = 517 nm), emission intensity, and exhibited identical XRD patterns, confirming its exceptional chemical stability. These results indicate that $CPTP_2MnBr_4$ is significantly more stable compared to lead-free double perovskites, such as $Cs_2Ag_{1-x}K_xIn_{0.875}Bi_{0.125}Cl_6$,[8] which exhibit phase instability and environmental degradation under similar conditions.

To further evaluate its stability under real-world environmental conditions, $CPTP_2MnBr_4$ was subjected to various stress tests, including 12 h of UV light exposure (254 nm), 150 °C heat exposure, X-ray irradiation, and storage at 100% relative humidity (RH%). As shown in Figure S11 (Supporting Information), no significant changes were observed in the PL or XRD characteristics under these conditions, confirming the material's robustness and stability.

Lastly, the photoluminescence quantum yield (PLQY) of $CPTP_2MnBr_4$ was measured under varying conditions. After 2500 h of storage under ambient conditions, the PLQY was 63.98%, comparable to the initial value of 62.8%, demonstrating excellent long-term stability (Figure S12, Supporting Information). PLQY measurements across a range of excitation wavelengths, as shown in Figure S13 (Supporting Information), further revealed consistent performance, supporting the material's high performance and versatility for optoelectronic applications.

After analyzing the structural and optical properties of $CPTP_2MnBr_4$, further experiments were conducted to evaluate

**ADVANCED
SCIENCE NEWS**

www.advancedsciencenews.com

**ADVANCED
MATERIALS**

www.advmat.de

Figure 3. a) XRD pattern of $CPTP_2MnBr_4$ before and after recrystallization. b) PL spectrum of $CPTP_2MnBr_4$ before and after recrystallization. c) Recrystallization mechanism under varying ethanol concentrations. d–g) SEM images showing particle size increase with higher ethanol concentrations. d) 0.5 mL g^{-1}, e) 1.0 mL g^{-1}, f) 1.5 mL g^{-1}, and g) 2.0 mL g^{-1}, respectively. h–k) Schematic of possible applications and their examples: (h) and (l) luminescent clay, (i) and (m) direct ink writing, (j) and (n) pattern printing, and (k) and (o) ink painting.

its reactivity with ethanol and investigate its phase stability. These results indicate that $CPTP_2MnBr_4$ dissolved in ethanol but recrystallized without the formation of impurities, thereby maintaining its crystal phase and optical properties after recrystallization. **Figure 3a** presents the XRD pattern of the powder sample after the reaction with ethanol, which remains consistent with the original polycrystalline powder, indicating that the material can undergo dissolution and recrystallization while preserving its structural integrity. This suggests that recrystallization, rather than inherent stability, allows the material to recover its original

crystal structure without degradation. In addition, the photoluminescence properties of $CPTP_2MnBr_4$ were evaluated to determine whether its reaction with ethanol affects its optical performance. As shown in Figure 3b, the luminescence properties were preserved with no noticeable degradation in the intensity or shifts in the excitation and emission wavelengths. This confirmed that the electronic states responsible for the luminescence remained unaffected by ethanol, further supporting the structural integrity and phase stability of the material under solvent interactions. Additionally, the stability of $CPTP_2MnBr_4$ in ethanol was also

**ADVANCED
SCIENCE NEWS**

www.advancedsciencenews.com

**ADVANCED
MATERIALS**

www.advmat.de

evaluated. A sample stored in ethanol for over a month was analyzed after drying. As shown in Figure S14 (Supporting Information), the comparison of PL and XRD results between the dried and pristine samples demonstrated no significant differences in intensity, emission profile, or crystal structure. This confirms that ethanol does not induce photoluminescence quenching or degradation of the material's photophysical properties, further supporting its potential for diverse applications.

The ability of $CPTP_2MnBr_4$ to dissolve and recrystallize without the formation of impurities highlights its ability to maintain its structural integrity and optical properties through solvent processing. This makes $CPTP_2MnBr_4$ particularly suitable for applications in which maintaining performance during solvent-based fabrication is critical, such as thin color-conversion layers for optoelectronic devices. Unlike other metal halide perovskites, which often degrade upon exposure to solvents, the capacity of $CPTP_2MnBr_4$ for impurity-free recrystallization reduces the need for complex encapsulation techniques, thereby simplifying the fabrication process.[12] This property is particularly valuable for real-world applications where stability under various environmental conditions is crucial. In comparison to other metal halide perovskites, which typically suffer from instability in solvent environments like ethanol, $CPTP_2MnBr_4$ demonstrates superior resilience. Although many perovskites exhibit significant degradation upon exposure to ethanol, the ability of $CPTP_2MnBr_4$ to recover its crystal structure after recrystallization makes it a more durable option for optoelectronic devices. This resilience to solvent exposure not only extends the longevity of the material but also opens up new opportunities for more flexible and solvent-tolerant device designs. To build upon the observed resilience of $CPTP_2MnBr_4$ in solvent environments, we conducted a series of experiments to further investigate the effect of the solvent concentration on its physical properties. The results revealed that variations in ethanol concentration directly influenced the morphology of the material. As shown in Figures S15 and S16 (Supporting Information), at lower ethanol concentrations, the material exhibited a clay-like consistency, indicating particle agglomeration, whereas at higher ethanol concentrations, it appeared more fluid, similar to ink. These findings highlight how the solvent concentration can significantly affect particle interactions and subsequent aggregation behavior.

The mechanism underlying the recrystallization process is illustrated in Figure 3c. When a small amount of ethanol is added, the solution quickly reaches saturation, leading to rapid nucleation. A high solute concentration in a small volume of solvent creates a supersaturated environment that promotes the formation of numerous small nuclei. However, because of the limited mobility of the solute molecules in this low solvent volume, the growth of these nuclei was restricted, resulting in a large number of small poorly formed crystallites. This condition also leads to nonuniform crystal growth because the limited solvent supply hinders efficient mass transport.

By contrast, when the amount of ethanol increased, the solute concentration decreased, and it took longer for the solution to reach saturation. This slower nucleation process leads to the formation of fewer nuclei. However, a larger solvent volume provides better mobility for the solute molecules, allowing the nuclei to grow into larger, more well-defined crystals. Ample solvent facilitates mass transport, resulting in more uniform and homogeneously grown crystals.

Supersaturation plays a critical role in this process as the driving force for nucleation. High supersaturation leads to rapid nucleation, producing many small nuclei, while lower supersaturation allows slower nucleation, enabling the growth of larger and better-formed crystals. Classical nucleation theory (CNT) emphasizes that nucleation rate and the size of critical nuclei are determined by supersaturation levels.[13] As such, solvent concentration effectively controls supersaturation, directly influencing nucleation and growth dynamics.

These differences in crystal size and uniformity, driven by supersaturation dynamics, highlight the solvent volume's crucial role in modulating nucleation and crystal growth processes. These findings indicate that the recrystallization process of $CPTP_2MnBr_4$ is highly sensitive to the amount of solvent used, which affects both the morphology and overall crystallization dynamics. At lower solvent volumes, nucleation dominated, resulting in smaller irregular crystals, whereas higher solvent volumes favored growth-dominated processes, producing larger and more uniform crystals. This understanding of solvent-controlled recrystallization mechanisms is valuable for optimizing the synthesis conditions of $CPTP_2MnBr_4$, particularly for tailoring its properties for specific applications such as ink-based painting or luminescent clays.

Figure 3d–g shows SEM images of $CPTP_2MnBr_4$ powder after adding varying amounts of ethanol, with ethanol concentrations of 0.5, 1.0, 1.5, and 2.0 mL g^{-1}, respectively. As described in the earlier mechanism, as the ethanol concentration increases from Figure 3d–g, particle size increases and uniformity improves. This confirms that the amount of ethanol significantly influences the crystallization of $CPTP_2MnBr_4$. These findings not only highlight the importance of solvent volume in controlling nucleation and growth but also open up new possibilities for practical applications. For instance, the ability of the material to change its physical state depending on ethanol concentration suggests potential uses in various fields. This versatility is demonstrated in Figure 3h–k,l–o, where we explore applications ranging from luminescent clay to ink-based painting techniques, showcasing the adaptability of the material in different contexts.

As shown in Figure 3h, when the ethanol concentration was low, the material exhibited clay-like agglomerations, which could be utilized as luminescent clay. When a small amount of ethanol was added, the particles partially dissolved, recrystallized, and agglomerated to form a plastic-like consistency. Once the ethanol evaporates, the material retains its form and hardens. Figure 3l demonstrates this property by forming a luminescent clay cube of ≈1 cm^3. We also demonstrated this property using a cookie mold to form a lion of ≈5 cm in size. Because of the viscosity and plasticity of the material in the presence of ethanol, as shown in Figure 3i, it can also be used for direct ink writing. For the direct ink writing process, $CPTP_2MnBr_4$ was mixed with ethanol at a ratio of ≈0.5 mL g^{-1} to create a homogeneous ink. This mixture was loaded into a 3 mL syringe without a needle. Consistent flow rate and pressure were manually applied by pressing the syringe plunger, allowing the material to be printed into specific shapes or thicknesses. By applying continuous pressure, the material can be printed into specific shapes or thicknesses. We printed the initials "HY" of Hanyang University with a size of

≈2–3 cm, as shown in Figure 3m. Furthermore, by increasing the amount of ethanol to make the material more fluid, pattern printing can be achieved using various pattern masks, as shown in Figure 3j. We employed a doctor blade to print the characters "funMat" engraved on a pattern mask, resulting in a pattern ≈3 cm in size, as illustrated in Figure 3n. Finally, when the amount of ethanol was significantly increased, most of the powder was dissolved in anhydrous ethanol, and the remaining material was evenly dispersed in the solvent. Using a brush to paint the light-green mixture, the material recrystallizes into a thin film as the ethanol evaporates, as shown in Figure 3k. This mixture was used to paint an image of a lion; the resulting artwork, ≈15 cm in size, is illustrated in Figure 3o, where the luminescent ink was used to draw a visible image under UV light after the ethanol had fully evaporated. These results provide valuable insight into the solvent-controlled recrystallization mechanism of $CPTP_2MnBr_4$ and demonstrate its potential for applications in optoelectronics, printing technologies, and luminescent materials. The stability of its structural and optical properties under different ethanol concentrations and its versatility in various applications make $CPTP_2MnBr_4$ a promising candidate for future material innovation.

This study proposes an innovative approach that utilizes the solvent-based plasticity of a new lead-free metal halide material, $CPTP_2MnBr_4$, to form uniform films without the use of binders. This method optimizes the thickness of the material and maximizes the light-emitting efficiency while preventing performance degradation caused by binders. This approach was applied to white light sources and scintillators to compare their efficiencies.

Before fabricating the WLED (white light emitting diode), it is important to balance the emission intensities of the green-emitting material $CPTP_2MnBr_4$ and the red-emitting material $K_2SiF_6:Mn^{4+}$. The emission colors of these materials are shown in Figure S17 (Supporting Information). PL was measured at various weight ratios of the luminescent materials, as shown in **Figure 4**a, and their emission colors were plotted in the CIE 1931 color space, as shown in Figure 4b. CIE(x,y) = (0.2021, 0.7005) represents the color coordinates of $CPTP_2MnBr_4$, while CIE(x,y) = (0.6179, 0.3053) represents those of $K_2SiF_6:Mn^{4+}$. The weight ratios used were 1:1, 2:1, 7:3, 9:1, 18:1, and 36:1. The results showed that the color coordinates in the CIE 1931 space changed linearly with varying weight ratios. An optimal balance of emission intensities was achieved at a 9:1 weight ratio, where the two luminescent materials contributed to white-light emission without overpowering each other. Note that this optimal ratio is attributed to the differing emission characteristics of the materials: $CPTP_2MnBr_4$, with its broad emission bandwidth (FWHM = 46 nm), requires a higher proportion to compensate for its energy distribution over a wider spectral range, while $K_2SiF_6:Mn^{4+}$, with its narrow bandwidth (FWHM = 7–10 nm), provides concentrated red emission with less material.

Using the proposed method, $CPTP_2MnBr_4$ and $K_2SiF_6:Mn^{4+}$ were successfully combined in a 9:1 ratio with anhydrous ethanol to create a clay-like material, which was applied to a 445 nm blue LED. Upon the evaporation of ethanol, a solidified color conversion layer was formed within ≈10 min (Figure S18, Supporting Information). For comparative analysis, luminescent materials were incorporated into a silicone elastomer (PDMS) matrix to fabricate WLEDs. To achieve optimal homogeneity, PDMS and the white-emitting powder were mixed at weight ratios of 1:1, 2:1, and 3:1 and ground for 3 min before being applied to the blue LED chip. The actual WLED chips fabricated using both approaches, along with conceptual images, are shown in Figure 4c.
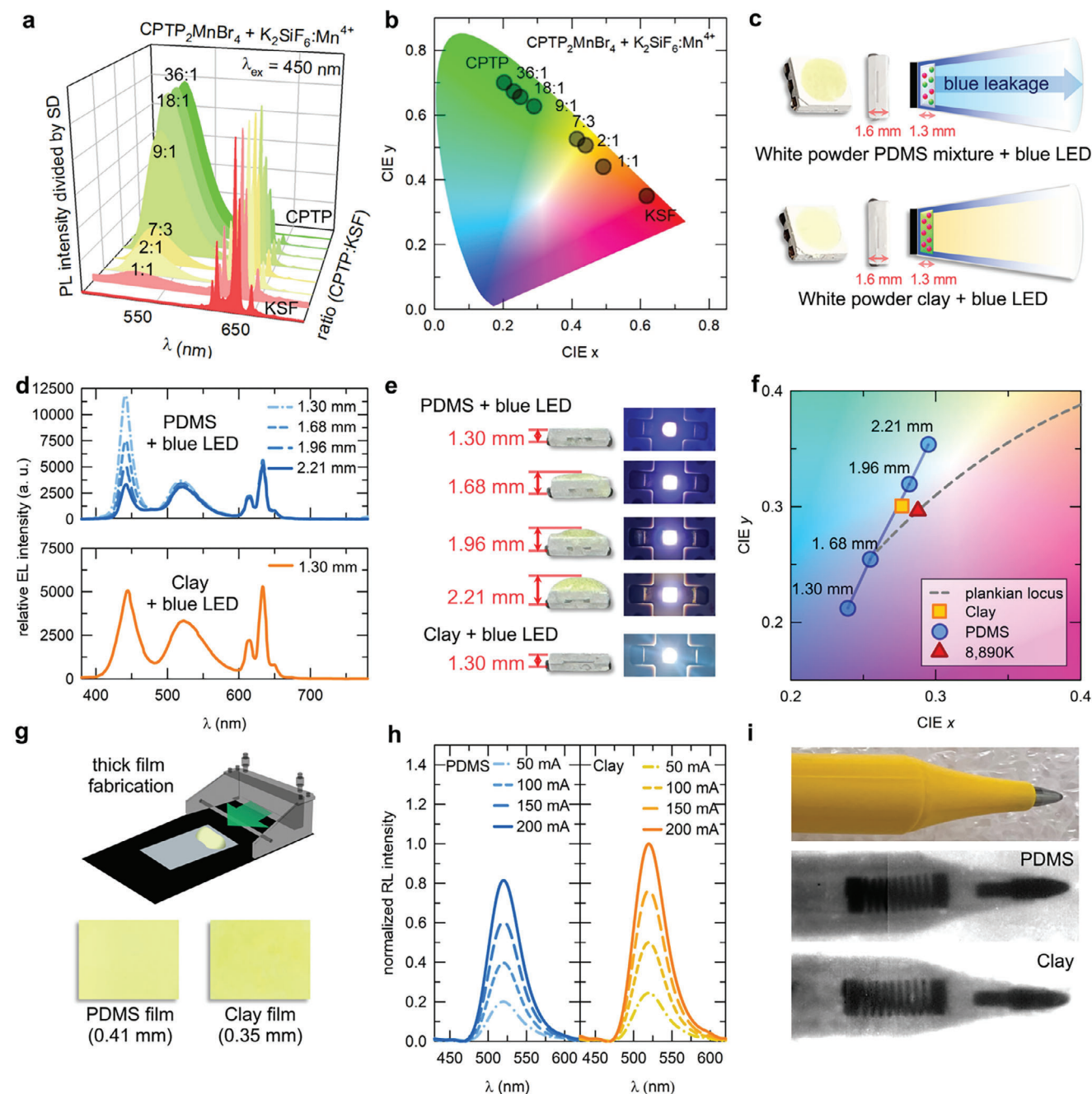
A performance comparison of WLEDs with different PDMS mixing ratios revealed significant findings. As shown in Figure S19 (Supporting Information), the 3:1 and 2:1 ratios resulted in thick color-conversion layers that still exhibited blue light leakage. By contrast, a 1:1 ratio produced stable and uniform white light. However, as shown in Figure 4d,e, even with a 1:1 ratio, a sufficiently thick color conversion layer (2.20 mm) was necessary to achieve effective white-light emission. However, the clay-based LED outperformed the PDMS-based LED, achieving efficient color conversion even at a thickness of 1.30 mm. This indicates that the clay-based material, with its high density and superior light conversion efficiency, enables enhanced white-light emission without the blue-light interference commonly observed in PDMS-based LEDs.

Figure 4f shows the superior chromaticity coordinates and correlated color temperature (CCT) of the clay-based system. For the same thickness (1.30 mm), the PDMS-based LED exhibited CIE(x,y) = (0.2392, 0.2121), corresponding to the blue region of the color space. For PDMS-based LEDs, achieving white light near the Planckian locus line required a thickness between 1.68 and 1.96 mm. By contrast, the clay-based LED reached chromaticity coordinates of CIE(x,y) = (0.2767, 0.3006) at a thickness of 1.30 mm, closely aligning with the Planckian locus line and corresponding to a white light emission of 8890K. These results demonstrate that clay-based LEDs can achieve efficient white-light emissions with minimal thickness, making them highly advantageous for compact, high-performance lighting applications.

Additionally, clay-based LEDs exhibit significant practical benefits over traditional PDMS- or resin-based systems because they do not require heat or UV curing to solidify the color-conversion layer. This simplifies the fabrication process while maintaining excellent performance. Furthermore, as shown in Figure S20 (Supporting Information), the clay-based LEDs demonstrated a linear increase in light output with increasing current from 50 to 200 mA, ensuring consistent performance under various operating conditions. These findings demonstrate the potential of the clay-based color conversion system to not only enhance the performance of WLEDs but also simplify the fabrication process, making it a highly promising candidate for next-generation lighting and display technologies. To further evaluate its performance, $CPTP_2MnBr_4$ clay film was compared with recently developed $CsPbBr_3$ NCs based resin film systems and PDMS-based films in terms of long-term stability and luminescent performance. As summarized in Table S5 (Supporting Information), $CPTP_2MnBr_4$ clay film demonstrated excellent long-term stability, maintaining its luminescent properties even after 120 days of storage at room temperature, outperforming polymer-based systems that often suffer from binder degradation. These results underscore the material's potential as a durable and efficient color conversion layer for advanced WLED and scintillator applications.

We also fabricated scintillator films without binders to compare their X-ray imaging performances. To confirm that $CPTP_2MnBr_4$ is suitable for X-ray imaging, its spectral sensitivity was examined. As shown in Figure S21 (Supporting

Figure 4. a) PL spectra of $CPTP_2MnBr_4$ and $K_2SiF_6:Mn^{4+}$ at various weight ratios. b) CIE 1931 color coordinates of $CPTP_2MnBr_4$ and $K_2SiF_6:Mn^{4+}$ at various weight ratios. c) Images of WLEDs fabricated using white-emitting powder based PDMS mixture and clay. EL spectra of d) PDMS + blue LED and clay + blue LED. e) Images of WLEDs with different thicknesses of PDMS mixture and clay. f) CIE 1931 color coordinates of PDMS + blue LED and clay + blue LED. g) Schematic of the fabrication method for PDMS and clay scintillator films. h) RL intensity comparison of PDMS and clay-type scintillator films. i) X-ray images of the ball-point pen using PDMS film and clay film.

Information), the radioluminescence (RL) spectrum of $CPTP_2MnBr_4$ matches well with the external quantum efficiency spectrum of the CMOS sensor. We used a doctor blade to prepare the PDMS and clay films. For the PDMS film, $CPTP_2MnBr_4$ (3 g) was mixed with PDMS (3 g) and a hardener (0.3 g), and the mixture was applied using a doctor blade, followed by heating at 80 °C for 1 h. The clay film was prepared

by mixing $CPTP_2MnBr_4$ (3 g) with ethanol (6 mL) to form a flowable clay, which was then dried after doctor blading. The thicknesses of the PDMS and clay films were 0.41 and 0.35 mm, respectively.

The RL intensities of the two films were compared by varying the X-ray tube currents. As shown in Figure 4h, despite being thinner, the clay film produced 1.25 times brighter light than the

ADVANCED
SCIENCE NEWS

www.advancedsciencenews.com

**ADVANCED
MATERIALS**

www.advmat.de

PDMS film. Additionally, both films exhibited a linear increase in RL intensity with increasing dose rate, as shown in Figure S22 (Supporting Information). Finally, the scintillator films were applied to an indirect X-ray imaging system to compare their performance. Figure S23 (Supporting Information) illustrates the structure of the indirect X-ray imaging system, which consists of an imaging target, a scintillator film, and an arrayed CMOS photodiode. The X-ray images were captured using a digital video output interface with a frame grabber. Static X-ray imaging was performed on both films. As shown in Figure 4i, the clay film produced high-contrast images of the internal structure of the ballpoint pen, whereas the PDMS film exhibited blurring and lower brightness. The resolution and sensitivity of the $CPTP_2MnBr_4$ clay and PDMS films were further evaluated through additional analyses. As shown in Figure S24 (Supporting Information), The X-ray imaging was performed using a tube voltage of 90 kV, a tube current of 200 mA, and a Source-to-Image Distance (SID) of 1 m, with an estimated dose rate of 445.08 mGy s^{-1}. The commercial $Gd_2O_2S:Tb^{3+}$ powder was purchased and fabricated into a film by mixing it with PDMS at a 1:1 ratio, followed by spin-coating. All films, including $CPTP_2MnBr_4$ clay, PDMS, and $Gd_2O_2S:Tb^{3+}$, were fabricated with a consistent thickness of 0.35 mm to ensure fair comparisons.

$$Sensitivity = \frac{Mean\ brightness\ (counts)}{Dose\ rate\ (mGy/sec)} \quad (5)$$

The sensitivity was calculated by normalizing the average brightness of the X-ray images to the dose rate. The $CPTP_2MnBr_4$ clay film achieved a sensitivity of 5.30 counts/mGy/sec, $\approx$86.6% of the $Gd_2O_2S:Tb^{3+}$ scintillator's sensitivity (6.12 counts/mGy/sec). In terms of resolution, modulation transfer function (MTF) analysis showed that the $CPTP_2MnBr_4$ clay and $Gd_2O_2S:Tb^{3+}$ films had identical resolution values of 1.3 lp mm^{-1} at an MTF value of 0.2, while the PDMS film exhibited a lower resolution of 0.7 lp mm^{-1}. These findings confirm that the $CPTP_2MnBr_4$ clay film offers competitive performance in both sensitivity and resolution compared to commercial scintillators. It is important to note that direct comparisons of MTF values with other studies are not meaningful due to the influence of several factors, including the Source-to-Image Distance (SID), pixel size and number of the imaging sensor, scintillator thickness and quality, and scintillation efficiency. Although Figure S25 (Supporting Information) shows that $CPTP_2MnBr_4$ has a relatively low X-ray absorption coefficient compared to commercial scintillators, this study demonstrates a novel binder-free approach for scintillator and WLED fabrication.

3. Conclusion

This study demonstrates that $CPTP_2MnBr_4$ is a promising lead-free metal halide material capable of forming uniform films without the need for binders owing to its unique solvent-based plasticity. By eliminating the binders, $CPTP_2MnBr_4$ addresses common challenges such as optical losses, increased layer thickness, and long-term stability issues found in conventional systems. Structural and optical analyses confirmed the high luminescence efficiency with a quantum yield of 83.42% in its single-crystal form, and the material maintained its structural and optical properties even after dissolution and recrystallization. These findings highlight the versatility of $CPTP_2MnBr_4$, particularly for applications such as luminescent clays, direct ink writing, pattern printing, and ink drawing. Furthermore, $CPTP_2MnBr_4$ shows significant potential to replace traditional binder-requiring systems in WLEDs and scintillators, where binder-free films can enhance performance and stability. While its application in WLEDs demonstrates its promise for lighting technologies, its binder-free approach also suggests potential for next-generation displays, including μ-LEDs, by enabling the development of high-performance and thinner color-conversion layers. Moreover, binder-free films can be fabricated via a simple drying process without the need for additional heat treatment or curing, which further simplifies the production process. Future research should focus on optimizing the material fabrication techniques for large-scale production and assessing their long-term stability under different environmental conditions to fully realize their industrial potential.

Conflict of Interest

The authors declare no conflict of interest.

Data Availability Statement

The data that support the findings of this study are available from the corresponding author upon reasonable request.

[1] a) A. R. Anwar, M. T. Sajjad, M. A. Johar, C. A. Hernández-Gutiérrez, M. Usman, S. Łepkowski, *Laser Photonics Rev.* **2022**, *16*, 2100427; b) T. Ma, J. Chen, Z. Chen, L. Liang, J. Hu, W. Shen, Z. Li, H. Zeng, *Adv. Mater. Technol.* **2023**, *8*, 2200632; c) J. E. Ryu, S. Park, Y. Park, S. W. Ryu, K. Hwang, H. W. Jang, *Adv. Mater.* **2023**, *35*, 2204947.

**ADVANCED
SCIENCE NEWS**

www.advancedsciencenews.com

**ADVANCED
MATERIALS**

www.advmat.de

[2] a) G. K. Grandhi, K. Mokurala, J. H. Han, H. B. Cho, J. Y. Han, W. B. Im, *ECS J. Solid State Sci. Technol.* **2021**, *10*, 106001; b) A. Fakharuddin, M. K. Gangishetty, M. Abdi-Jalebi, S.-H. Chin, A. R. bin Mohd Yusoff, D. N. Congreve, W. Tress, F. Deschler, M. Vasilopoulou, H. J. Bolink, *Nat. Electron.* **2022**, *5*, 203; c) B. Zhao, M. Vasilopoulou, A. Fakharuddin, F. Gao, A. R. b. Mohd Yusoff, R. H. Friend, D. Di, *Nat. Nanotechnol.* **2023**, *18*, 981.

[3] a) T. Samanta, N. Mukurala, N. S. M. Viswanath, J. H. Han, H. B. Cho, J. W. Min, S. W. Jung, Y. Park, W. J. Chung, W. B. Im, *Optical Materials: X* **2023**, *18*, 100238; b) C. H. Chen, S. N. Cheng, L. Cheng, Z. K. Wang, L. S. Liao, *Adv. Energy Mater.* **2023**, *13*, 2204144; c) M. Ren, X. Qian, Y. Chen, T. Wang, Y. Zhao, *J. Hazard. Mater.* **2022**, *426*, 127848.

[4] a) J. H. Han, T. Samanta, Y. M. Park, H. J. Kim, N. S. Manikanta Viswanath, H. W. Kim, B. K. Cha, S. B. Cho, W. B. Im, *ACS Energy Lett.* **2022**, *8*, 545; b) J. Li, J. Duan, X. Yang, Y. Duan, P. Yang, Q. Tang, *Nano Energy* **2021**, *80*, 105526; c) F. Zhang, Z. Ma, Z. Shi, X. Chen, D. Wu, X. Li, C. Shan, *Energy Mater. Adv.* **2021**, *38*, 5198145; d) J. W. Min, T. Samanta, A. Y. Lee, Y. K. Jung, N. S. M. Viswanath, Y. R. Kim, H. B. Cho, J. Y. Moon, S. H. Jang, J. H. Kim, *Small* **2024**, *20*, 2402951; e) J. H. Han, T. Samanta, H. B. Cho, S. W. Jang, N. Viswanath, Y. R. Kim, J. M. Seo, W. B. Im, *Adv. Mater.* **2023**, *35*, 2302442.

[5] a) S. Si, L. Huang, X. Zhang, J. Wang, *Adv. Photonics Res.* **2022**, *3*, 2100146; b) A. Gaurav, C.-Y. Tsai, G.-W. Wang, H.-Y. Tsai, Z. T. Ye, C.-F. Lin, *Photonics Res.* **2023**, *11*, 925.

[6] a) T. Güner, Izmir Institute of Technology, Turkey **2018**; b) S. R. Lee, J. C. Lo, M. Tao, H. Ye, *From LED to solid state lighting: principles, materials, packaging, characterization, and applications*, John Wiley & Sons, Hoboken, NJ **2021**.

[7] H.-S. Lee, J. H. Hwang, T.-Y. Lim, J.-H. Kim, D.-W. Jeon, H.-S. Jung, M. J. Lee, *J. Korean Ceram. Soc.* **2015**, *52*, 229.

[8] P. Zhu, S. Thapa, H. Zhu, S. Wheat, Y. Yue, D. Venugopal, *J. Alloys Compd.* **2023**, *960*, 170836.

[9] L. Mao, P. Guo, S. Wang, A. K. Cheetham, R. Seshadri, *J. Am. Chem. Soc.* **2020**, *142*, 13582.

[10] X. Zhao, M. Wu, H. Liu, Y. Wang, K. Wang, X. Yang, B. Zou, *Adv. Funct. Mater.* **2022**, *32*, 2109277.

[11] Q. Ren, J. Zhang, Y. Mao, M. S. Molokeev, G. Zhou, X.-M. Zhang, *Nanomaterials* **2022**, *12*, 3142.

[12] a) S. Svanstrom, T. J. Jacobsson, G. Boschloo, E. M. Johansson, H. Rensmo, U. B. Cappel, *ACS Appl. Mater. Interfaces* **2020**, *12*, 7212; b) B. Dou, L. M. Wheeler, J. A. Christians, D. T. Moore, S. P. Harvey, J. J. Berry, F. S. Barnes, S. E. Shaheen, M. F. van Hest, *ACS Energy Lett.* **2018**, *3*, 979; c) M. Masri, A. Hezam, K. Alkanad, K. Prashantha, S. Manjunath, F. Masri, T. F. Qahtan, K. Byrappa, *Colloids Surf. A* **2024**, *687*, 133387.

[13] a) J. Kim, Y. Kimura, B. Puchala, T. Yamazaki, U. Becker, W. Sun, *Science* **2023**, *382*, 915; b) P. T. Cardew, *Cryst. Growth Des.* **2023**, *23*, 3958; c) S. Karthika, T. Radhakrishnan, P. Kalaichelvi, *Cryst. Growth Des.* **2016**, *16*, 6663.

2415247 (10 of 10)